Remote Sensing of Environment 222 (2019) 50–64

Contents lists available at ScienceDirect

Remote Sensing of Environment

journal homepage: www.elsevier.com/locate/rse

Basin- to mesoscale surface circulation of the Western Mediterranean manifested by satellite-derived data products

Svetlana Karimova

Department of Astrophysics, Geophysics, and Oceanography, University of Liege, Allée du 6 Août, 19, Bât. B5a, 4000 Liège, Belgium

ARTICLE INFO

Keywords:
SST
SLA
Geostrophic currents
Mesoscale eddies
Eddy detection
Mediterranean Sea
GlobCurrent

ABSTRACT

In this article, there is an overview of the potential of different (mostly altimetry-derived) products for manifesting features of basin- and mesoscale circulation of the Western Mediterranean Basin. In terms of detection of mesoscale eddies and larger gyres, the comparison was performed between eddy statistics extracted directly from fields of sea surface temperature (SST), on the one hand, and reconstructed from different scalar and vector altimetry-derived fields, on the other hand. Among the products being analysed, there are fields of (i) sea level anomaly (SLA), (ii) geostrophic currents, and (iii) finite size Lyapunov exponents (FSLE). Comparison of the eddy statistics provided by such different data sources revealed that altimetry-based techniques tended to overestimate the number of big cyclones and thus failed to reproduce cyclonic/anticyclonic eddy asymmetry which was shown by fields of SST. Defining the spatial scale of eddies via altimetry-based techniques seemed particularly problematic. FSLE product analysed in the study showed significant disagreements with vortical structures observed in fields of SST both in terms of the spatial scale and the sign of rotation. In order to scrutinize basin-scale features of surface circulation in the region of interest, fields of (i) geostrophic currents, (ii) total currents reconstructed by the GlobCurrent project, and (iii) surface currents provided by the reanalysis technique were analysed. As a result of the comparison performed, a conclusion was made on the complementarity of the datasets analysed.

1. Introduction

The role of surface currents in driving local biogeochemical cycles in a marine basin can hardly be overestimated. Coherent structures, or eddies, are particularly important in this respect. Due to their long lifetimes and associated with them high horizontal velocities, such structures greatly affect the statistical properties of the turbulence field and actively participate in horizontal water transport. Vertical fluxes induced by mesoscale eddies are much smaller than horizontal ones, but still important for the dynamics of a marine ecosystem. It is believed that cyclonic eddies stimulate biomass growth as a result of remarkable upwelling of nutrient-rich water in their cores (e.g. McGillicuddy Jr et al., 1998). Unlike cyclonic eddies, anticyclonic ones are considered to enhance bioproductivity due to strong upward velocities on their edges (Casella et al., 2011). Shallow-water mesoscale vortices on a coastal slope, in their turn, generate a complex pattern of strong vertical velocities, thereby also providing a link between nutrient-rich deep waters and the nutrient-depleted upper layer (Zavala Sanson and Provenzale, 2009).

Satellite data offer wide opportunities for observing mesoscale eddies. There exist two quite different ways for providing such observations. The first one is performed through the use of different types of satellite imagery retrieved at thermal infrared, visible or microwave parts of the electromagnetic spectrum. Another option for detecting eddy manifestations is to analyse fields of sea level anomaly (SLA) and its derivatives.

It is obvious that eddy detection results provided by such different techniques cannot entirely agree due to a number of objective and subjective reasons. First, currents involved into a vortical movement (and noticed in a satellite image) might be not yet geostrophically balanced and as a result cannot have a corresponding imprint in a field of SLA. Second, SLA signal can be influenced by the character of vertical stratification of underlying water, which is typically unknown during the inspection of fields of SLA. Third, a similar impact can be performed by some atmospheric phenomena which were not resolved or considered by the atmospheric corrections applied to SLA data products.

The factors just mentioned can lead to the situation when even a bigger eddy visualized in an image might be not represented by a reconstructed field of SLA (some examples can be found in (Karimova, 2018)), Since the ability of satellite-derived fields to resolve eddies of different spatial scales strongly depends – among other factors – on the spatial resolution of data being analysed, discrepancies between

---

E-mail address: svetlana.karimova@uliege.be.

https://doi.org/10.1016/j.rse.2018.12.004
Received 22 October 2017; Received in revised form 23 November 2018; Accepted 3 December 2018

satellite imagery and fields of SLA increase if one considers the smaller spatial scales. Thus, thermal infrared images with 1-km pixel dimension can visualize eddies exceeding 20–30 km in diameter, provided there are enough tracers present on the water surface or in the upper water layer (Karimova, 2013, 2017a, 2017b). Gridded SLA products, however, were reported to resolve only those eddies that exceed approx. 70 km in diameter (Chelton et al., 2011). This limitation means that fields SLA might be not the best data source for studying mesoscale eddies in small marine basins like, e.g. the Mediterranean Sea where typical values of the Rossby radius are of 10–18 km (Escudier et al., 2016).

Additional concern about the credibility of altimetry-derived eddy statistics is provided by the fact that eddy detection techniques applied to fields of SLA and/or of its derivatives are typically being quite subjective multiparametric procedures and as such they require stages of a particularly careful calibration and validation. Such stages, however, are usually being omitted.

In this article, we thus provide a methodological comparison of eddy detection results based on an analysis of altimetry-derived products, on the one hand, and satellite imagery, on the other hand. The aim of the study is to compare the performance of different eddy detection techniques: (i) a direct observation of eddies in satellite thermal infrared imagery, (ii) an analysis of closed contours in fields of SLA, (iii) a retrieval of winding patterns in vector fields of geostrophic surface currents, and (iv) an inspection of fields of finite size Lyapunov exponents (FSLE). Besides the reasons mentioned above, additional motivation for such a comparison is provided by significant discrepancies in the eddy statistics reported upon the usage of these different methods. Thus, from an analysis of satellite imagery it was inferred that strong anticyclonic dominance usually took place among mesoscale eddies of inner and marginal seas (Zatsepin et al., 2003; Font et al., 2004; Karimova, 2011, 2013, 2017a). The SLA-based methods, however, report on similar characteristics of cyclonic and anticyclonic eddies in such marine basins (Isern-Fontanet et al., 2006; Kubryakov and Stanichny, 2015).

In order to take a closer look at the manifestation of eddies by different satellite-derived data, a two-year long dataset of quasi-simultaneously obtained daily fields of sea surface temperature (SST) and altimetry products is being analysed. As a region of interest, the Western Mediterranean Basin was chosen. This area is known for its intensive eddy activity resulting in the appearance a variety of eddies up to 200 km in diameter (Millot, 1987).

In order to investigate basin-scale surface circulation features in the region of interest, we perform a comparison of different data products on surface currents in that area as well.

The rest of the article is organised as follows. In Section 2, surface circulation in the region of interest is being briefly characterised. Section 3 provides a description of the datasets used. In Section 4, there is a comparison of eddy statistics retrieved from different data products. Potential of different datasets for manifestation of basin-scale circulation features in the region of interest are being analysed in Section 5. Finally, Section 6 concludes the results of the study.

2. Study area

The area of the present study is the Western Mediterranean Basin, which is the western part of the Mediterranean Sea including the Algerian and Liguro-Provençal Basins as well as the Alboran, Balearic, and Tyrrhenian Seas. Topographically, the Western Mediterranean Basin consists of a series of deep depressions connected to each other, with a mean depth of about 1500 m (Fig. 1).

There exist different visions of generalized surface circulation in the Western Mediterranean. Mostly they are more or less modified versions of the sketches presented by Millot in 1987 and 1999. Most of the authors who provide such generalized schemes seem to agree that the main current in the area is the Algerian Current, which is mainly governed by the thermohaline processes. Since the Western Mediterranean is characterised by the great excess of evaporation, in order to compensate the loss of water, relatively fresh water from the Atlantic Ocean enters the basin through the Strait of Gibraltar (Millot, 1987). On arrival, Atlantic water flows along the southern coast of the basin giving rise to the Algerian Current. In the area to the south of Sardinia, the flow divides into two branches, one continuing eastward to the Eastern Mediterranean Basin through the Strait of Sicily and the other being inflected northward into the Tyrrhenian Sea and eventually reaching the Liguro-Provençal Basin (Millot, 1999). Another strong current in the area (the North Current) transports water along the northern coast of the Western Mediterranean and finally gets back to the Alboran Sea (Millot, 1999). Thus, in general surface circulation in the Western Mediterranean is composed by a large scale permanent cyclonic gyre.

If we consider surface currents of the Western Mediterranean in greater detail, we would reveal certain disagreements between schemes of surface circulation provided by different authors. For example, smaller cyclonic gyres (like the ones in the Tyrrhenian and Balearic Seas) are usually not mentioned in generalized schemes. Another contradicting point concerns surface circulation in the vicinity of Sardinia. In some publications, there is anticyclonic circulation shown around Sardinia (e.g. Buffett et al., 2013; Nielsen, 1912; Sverdrup et al., 1944). Some other sources (e.g. Pinardi et al., 2015; Poulain et al., 2012), however, indicate dominance of southward currents both to the west and to the east of Sardinia. Due to such discrepancies in the existing references to the surface circulation scheme of the Western Mediterranean Basin, in the present study we will compare the evidence provided by different data products aiming at better understanding of general surface circulation in the Western Mediterranean.

As far as mesoscale vortical structures are concerned, the biggest, most persistent, and most studied eddies of the Western Mediterranean Basin are those observed in the Alboran Sea and so they are frequently referred to as Alboran Eddies or Alboran Gyres. These are one or two anticyclonic gyres with a diameter up to 150 km associated with sharp thermohaline fronts caused by the appearance of Atlantic water in the Alboran Sea (Millot, 1987; Font et al., 2002). In most cases these eddies are indicated in the schemes of surface circulation starting from the one by Millot (1987).

In the Algerian Basin, anticyclonic eddies with a diameter of about 150 km come into being as a result of the hydrodynamic instability of the Algerian Current. These gyres are usually also marked in the schemes of surface circulation (e.g. Millot, 1987, 1999; Buffett et al., 2013; Poulain et al., 2012), but their exact locations differ from one scheme to another. This situation is being further complicated by the fact that such eddies tend to propagate eastward along the Algerian coast at a speed of few kilometers per day (Puillat et al., 2002). As a result, revealing of locations where large eddies are particularly frequently observed is getting a difficult task. It was also reported that eddies can detach from the Algerian slope and propagate northwards to the middle of the western part of the Western Mediteranean (Puillat et al., 2002; Salas et al., 2002; Taupier-Letage and Millot, 1988).

Data on appearance of mesoscale eddies of smaller spatial scales (less than approx. 100 km in diameter) in the study area are still very sparse. Isern-Fontanet et al. (2006) studied mesoscale eddies manifested in fields of SLA of that area and showed that among vortices with high values of amplitude, energy, and size, anticyclonic eddies prevailed while in general approximately similar numbers of cyclonic and anticyclonic vortices were discovered.

Escudier et al. (2016) analysed results of a numerical hydrodynamic model along with fields of SLA. The model revealed a multitude of eddies with a diameter of about 40–50 km. The average diameter of eddies retrieved from the SLA maps in that study was approx. 60 km. The lifetime of eddies was found to be quite short, with a median value of 13 days (Escudier et al., 2016). It is noteworthy that while describing the statistics on eddies found in fields of SLA, Escudier et al. (2016)

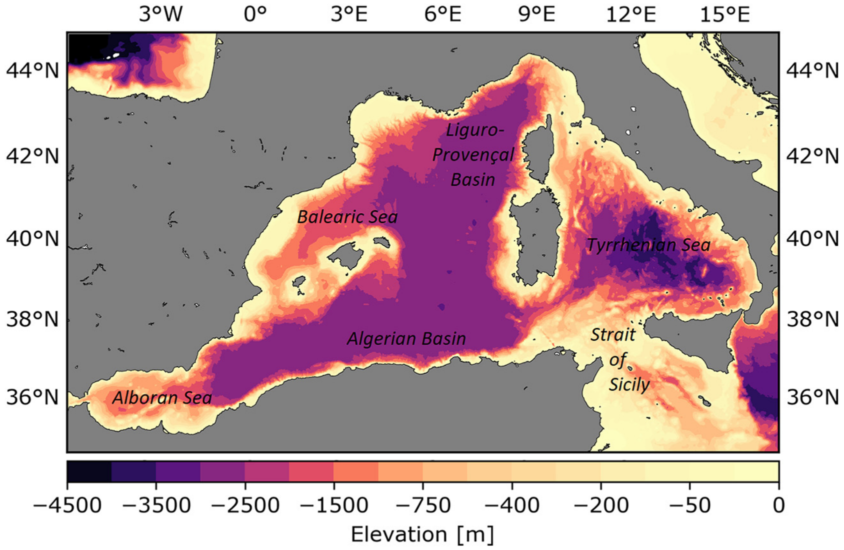

Fig. 1. Elevation map of the study area.

never clarified if they meant anticyclonic or cyclonic eddies.

As for the usage of satellite imagery, mesoscale eddies in this area were tackled in the works of Karimova and Gade (2016) and Karimova (2017a, 2017b, 2018). The point at which altimetry- and imagery-derived statistics differ most is the ratio between cyclonic and anticyclonic vortices of the same spatial scale. This point will be thoroughly considered further in the article.

Another remarkable feature of mesoscale eddy activity in the region of interest is its strong seasonal variability. In winter, due to intensive wind-induced mixing, the upper mixed layer is getting quite deep (at places over 2000 m), and the turbulent regime during that period can be characterised as three-dimensional. As a result, from December to late March – early April, vortical structures in the region of interest are rather small. Since such effective vertical mixing leads to intensive blooming of phytoplankton species, around the spring season fields of chlorophyll-a concentration (Chl-a) provide impressive snapshots of surface water stirring. Such an example of chaotic water stirring typical for the cold season is given in Fig. 2(a). Chl-a field presented in the figure was retrieved from data captured by Moderate Resolution Imaging Spectroradiometer (MODIS) Aqua on 23.02.2014.

During the warm season (which lasts typically from April to November), the upper water layer is getting restratified, so that the mixed layer gets as thin as 50 m or even less. Under such circumstances, the turbulence regime can be approximated by the two-dimensional model and characterised by the corresponding inverse energy cascade. Such energy cascade, in its turn, favours the appearance of a variety of well-developed large-scale vortices (mostly anticyclonic). An example of Chl-a field that is showing surface circulation features typical for the warm season can be found in Fig. 2(b). This Chl-a field was captured by Visible Infrared Imaging Radiometer Suite (VIIRS) on board the Suomi National Polar-orbiting Partnership (Suomi NPP) weather satellite on 28.06.2014.

From the biogeochemical point of view, the Mediterranean Sea is considered one of the largest oligotrophic areas in the world. In comparison with the Eastern Mediterranean Basin, the Western one is nevertheless quite productive due to seasonal deep convection and wind forcing provided by the Mistral winds (Barale et al., 2008). As it was just demonstrated by Fig. 2(a) and (b), during phytoplankton blooming events visible-range satellite imagery (e.g. fields of Chl-a) can consequently reveal quite remarkable patterns of surface circulation in the Western Mediterranean. In the present study, we, however, perform an analysis of thermal infrared rather than visible-range satellite imagery, since the former stay quite informative all year round and not only during phytoplankton blooming events.

3. Data and methods

3.1. Front detection

In order to reveal locations of strongest and most persistent thermal fronts in the study area, we used daily gap-free gridded Level 4 (L4) fields of SST produced by Consiglio Nazionale delle Ricerche (CNR), Italy, and provided by the Copernicus Marine Environment Monitoring Service (CMEMS). Spatial resolution of these SST data is 0.0625°; for the study area, that results in a resolution cell of approx. 5.3 km per 6.9 km. Temporal coverage of this dataset is from 2008 to 2015, inclusively. Technically speaking, most persistent thermal frontal zones were associated with areas where greatest values of seasonally or totally averaged numerical gradient of SST were encountered.

3.2. Eddy detection

3.2.1. Direct observations of eddies in thermal infrared imagery

As ‘ground truth’ for detection of mesoscale eddies in the region of interest we used thermal infrared imagery. As it was mentioned earlier, such images are not as informative as e.g. fields of Chl-a during a phytoplankton blooming event, but they allow observing large mesoscale eddies throughout all seasons.

Eddy detection was performed using an SST product different from the one applied for the front detection, namely a Level 3 super-collated (L3S) product. This another product was chosen due to different needs of the two procedures. Since just very general information on thermal fronts was needed, an easy-to-use gridded L4 product, having all artefacts removed, perfectly suited the front detection procedure. For identifying individual eddy manifestations, however, momentarily snapshots of SST were required. In that case, possible imperfectness and artefacts present in images did not matter, while a manned eddy detection procedure was applied.

L3S is a multi-sensor product generated by CNR and distributed by CMEMS. It is created from bias-corrected L3 mono-sensor (collated) products at the spatial resolution of 0.01° (with a resolution cell of approx. 0.8 km per 1.1 km). If the resolution of the collated image is higher than 0.01 °, the degradation of the resolution is performed by averaging the best quality data. Otherwise, the collated pixels are associated with the nearest neighbours without interpolation or artificial increase of the spatial resolution of the final product. The original data

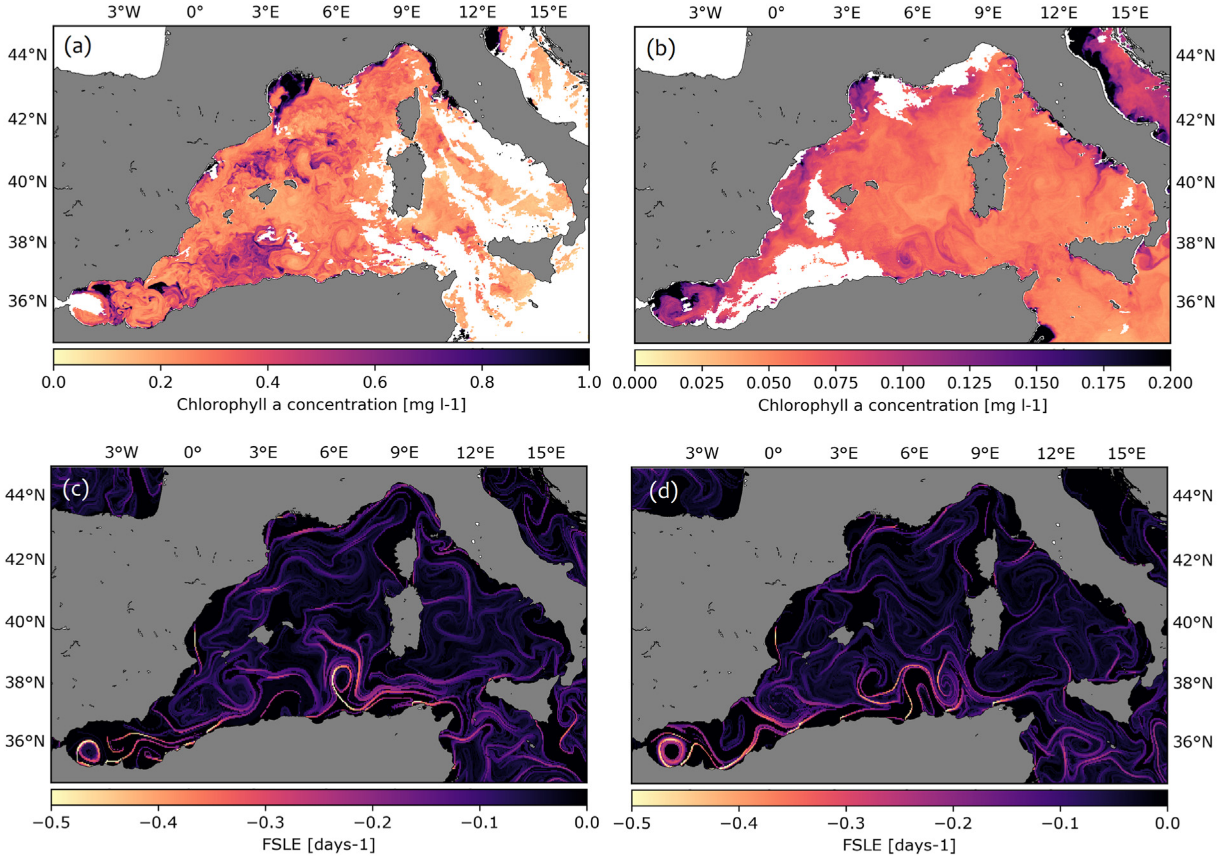

Fig. 2. Examples of surface water stirring in the study area during the cold (a) and warm (b) seasons manifested by fields of Chl-a captured on 23.02.2014 by MODIS Aqua (a) and on 28.06.2014 by VIIRS (b), as well as fields of FSLE for the 24.02.2014 (c) and 28.06.2014 (d). (For interpretation of the references to color in this figure legend, the reader is referred to the web version of this article.)

used for computation of L3S fields were obtained by the AVHRR instruments on board the METOP-A, NOAA-18, and NOAA-19 satellites. The product is provided with a daily temporal resolution.

The temporal coverage of the analysed dataset was limited by two years, 2008 and 2014. These years were picked with the aim of performing some further comparisons of eddy detection results with along-track SLA data from different satellite altimetry missions (not included in the present article). It is rather unfortunate that the time coverage of data being analysed in this study is discontinuous and comprising only the years of 2008 and 2014. It would be possible to have analysed additional data and hence to get results for some sequential years, but that would provide significant additional and probably not necessary workload.

In the present study, we used a manual eddy detection method. There is typically a great variety of ways in which vortical structures get visible in a satellite-derived image. As a result, application of fully automated eddy detection procedures to an analysis of satellite imagery is still problematic, and only manual processing of images by an experienced operator would provide reliable results (at least until the advance of well-developed machine-learning techniques).

Being manifested in thermal infrared images, eddies usually look like one of the features listed below:

- a circular-shaped patch with seemingly homogeneous distribution of SST inside; such patterns are mostly associated with large eddies along the southern coast of the region of interest;
- a circular or elliptical patch with a spiral-like structure;
- a narrow flow with a contrast of temperature bordering a circular-shaped patch;
- a narrow flow winding into a spiral or a part of such flow.

As a measure of the eddy spatial scale, we used a diameter length for circular-shaped eddies. For elliptical eddies, it would be beneficial to have fixed the length of both axes, but that would nearly double the manual workload needed for defining the spatial scale of eddy manifestations found. It was therefore decided to have fixed only the length of the bigger axes.

If thermal contrasts inside an eddy pattern allowed, location of the centre of the eddy was directly figured out. Otherwise, it was the geometrical centre of the patch that was considered an eddy centre.

Patches that manifest eddies in SST imagery (or at least contour the edges of an eddy) usually show a tendency to wind into a spiral, so in most cases defining the sign of eddy rotation do not provide difficulties. Additional characteristic feature of a big anticyclone that can be useful while interpreting satellite imagery is the presence of smaller-scale attached cyclonic eddies on the periphery of big anticyclonic eddies (Ginzburg et al., 2002; Karimova, 2011, 2013). A special advantage of dealing with mesoscale eddies, in comparison with smaller submesoscale vortices, is that mesoscale features can be observed in a series of images. Thus, in case of any doubts raising in the course of an image analysis, there is a possibility to have a look at earlier and/or later images of the same region. Finally, if for a certain eddy manifestation, it was not possible to define its spatial scale or sign of rotation, such manifestation was disregarded. We could easily afford that, since there were many and many eddies that could not be seen in images due to, for example, the presence of cloud cover over the region of interest.

Following the methodology described above, SST images obtained in 2008 and 2014 were inspected visually and for eddy manifestations noted, their spatial scale, location of the eddy centre, and sign of rotation were defined.

3.2.2. *Eddy detection in fields of SLA*

An altimetry-derived data product used in the study, namely fields of SLA, has been created by the Collecte Localisation Satellites Group (CLS), Toulouse, France, and distributed by CMEMS. The product provides anomalies of sea surface height (SSH) referenced against the 20-year mean value. In order to gain this product, data from different altimeter missions were homogenized using the Jason-2 mission as the reference one. Such obtained combined measurements were smoothed applying a 12-week time window, and the resulting dataset was cross-validated, filtered from the residual noise, and sub-sampled. Finally, gridded fields of SLA were calculated from the along-track measurements via an application of an optimal interpolation algorithm. Spatial resolution of the gridded product is 0.125 °(approx. 10.9 km per 13.9 km). Similar to SST imagery used in the study, fields of SLA were provided with a daily temporal resolution.

There have been multiple techniques developed for extracting possible eddy manifestations from fields of SLA. The most popular approach is probably the one which implies interpreting a possible eddy manifestation as a closed contour in a contoured dynamical field with a significant local extremum inside the contour. This approach is based on the assumption that a well-developed mesoscale eddy being in a geostrophic balance should have a corresponding local anomaly of sea level in its centre, which is positive for an anticyclonic eddy and negative for a cyclonic one. Traditionally in such kind of an analysis, there are either fields of SLA (Palacios and Bograd, 2005; Stegmann and Schwing, 2007; Chelton et al., 2011; Kurian et al., 2011; Mill et al., 2015), or SSH (Halo et al., 2013), or those of the Okubo-Weiss parameter that are being scrutinized. The Okubo-Weiss parameter, W, is defined as

$$W = s_n{}^2 + s_s{}^2 + \omega^2$$

where $s_n = \partial u/\partial x - \partial v/\partial y$ and $s_s = \partial v/\partial x + \partial u/\partial y$, $\omega = \partial v/\partial x - \partial u/\partial y$,while zonal and meridional components of the surface currents field u and v, respectively, are derived using the geostrophic approximation (e.g. Isern-Fontanet et al., 2006):

$$u = -g/f\ \partial h/\partial y,\ v = g/f\ \partial h/\partial x, \tag{1}$$

where g is gravitational acceleration, f is the Coriolis parameter, and h is a SLA value. W provides a measure of relative dominance of strain over vorticity and as such is widely used in the studies of two-dimensional turbulence. Since vortices are regarded as single connected regions of concentrated vorticity dominating over strain, the Okubo–Weiss parameter offers a basis for a vortex identification criterion as a region with negative values of the Okubo-Weiss parameter. This criterion is frequently used for eddy detection in altimetry- and numerically-derived fields (Isern-Fontanet et al., 2006; Chelton et al., 2007; Chaigneau et al., 2008; Henson and Thomas, 2008; Sangrà et al., 2009; Souza et al., 2008; Halo et al., 2013; Mill et al., 2015).

Similar to the Okubo-Weiss parameter, the Q-parameter, Q, represents the second invariant of the velocity gradient tensor and characterizes local balance between shear strain rate and vorticity magnitude (Isern-Fontanet et al., 2003). For the planar flows, it can be expressed in the following form:

$$Q = -(\partial u/\partial x)^2 - \partial v/\partial x\ \partial u/\partial y$$

Since at positive Q the rotation dominates over the deformation, an eddy is supposed to exist in regions where Q is positive and relatively large. This parameter has been used for eddy detection in the Algerian Basin of the Western Mediterranean (Isern-Fontanet et al., 2003), in the main upwelling systems of the World Ocean (Morrow et al., 2004), and in the California Current System (Kurian et al., 2011).

In order to achieve better eddy detection results, in some works there was a combination of criteria used. Thus, Halo and co-authors (2013) registered only those contours where the values of both SLA and the Okubo-Weiss parameter were meeting certain requirements.

Upon a preliminary study, it was discovered that for the Western Mediterranean Basin using fields of the Okubo-Weiss parameter instead of those of SLA did not provide any significant benefits (Karimova, 2016, 2018). In the present article, the closed contour approach is therefore being applied solely to fields of SLA.

3.2.3. *Eddy detection in vector fields*

According to another approach to eddy detection (frequently referred to as a geometrical group of methods), it is a flow field that is being analysed, in order to detect possible eddy manifestations. Thus, within a so-called winding-angle approach the curvature of the streamlines is used for detecting eddies. Such a method was proposed by Sadarjoen et al. (1998) and nowadays is frequently used for eddy extraction from altimetry-based or numerically-derived fields of surface currents (Chaigneau et al., 2008, 2009; Souza et al., 2008; Kubryakov and Stanichny, 2015; Pegliasco et al., 2015).

Instead of the geometry of streamlines, it can be the vector geometry in a field of surface currents to be analysed (Nencioli et al., 2010). In the present study, we are testing this method as well. For that, zonal and meridional components of a field of surface currents u and v were derived from the aforementioned SLA product using the geostrophic approximation (1).

In order to find possible eddy manifestations in thus obtained fields of geostrophic currents, they were searched for patterns satisfying the two criteria from (Nencioli et al., 2010), namely that there should be (i) a local minimum of the velocity magnitude and (ii) corresponding nearby reversal of the velocity vectors. For the study area, we introduced one more requirement, namely that the maximum speed of the currents within the pattern being considered should be greater than $0.1\ \mathrm{m{\cdot}s^{-1}}$.

3.2.4. *Eddy detection in fields of FSLE*

One more eddy detection method tested in the present study is based on an analysis of fields of multimission altimetry-derived backward-in-time finite-size Lyapunov exponents (FSLE). Such fields were computed in collaboration between CLS, LOcean, Centre of Topography of the Oceans and the Hydrosphere (CTOH), and Centre National d'Etudes Spatiales (CNES) in the framework of the joint SALP (Service d'Altimetrie et Localisation Precise) and DUACS (Data Unification and Altimeter Combination System) project. The product is being distributed by the CNES service AVISO+. The spatial resolution of FSLE fields is 0.04° (approx. 3.5 km per 4.4 km); the temporal one is 3 days.

Lyapunov exponents are defined as the averaged over infinite time exponential rate of separation of fluid parcels initially separated infinitesimally. FSLE were introduced for studying non-asymptotic dispersion processes, which are particularly appropriate for an analysis of horizontal transport in closed areas. It was shown that ridges of FSLE can be associated with hyperbolic Lagrangian coherent structures (LCSs) (Karrasch and Haller, 2013). For more details on the application of Lyapunov exponents for studying surface currents and LCSs in particular one can refer to (Beron-Vera et al., 2008; d'Ovidio et al., 2009).

Similar to SST imagery used in the study, eddy detection in fields of FSLE was performed manually.

3.3. *Analysis of surface currents*

3.3.1. *Geostrophic currents*

Fields of geostrophic currents analysed in this study were retrieved from the SLA data described in Subsection 3.2.2. The temporal coverage of the dataset is from 1993 to 2015.

3.3.2. *GlobCurrent total currents*

An alternative product for assessing surface currents in the region of interest was provided by fields of total (namely geostrophic plus Ekman) currents at 15-m depth calculated within the GlobCurrent project (http://www.globcurrent.org/). The GlobCurrent project is aimed at a synergetic use of satellite and in situ data for developing new products on ocean surface currents. The datasets involved include data from satellite-tracked drifting buoys, estimates of geostrophic surface currents by satellite altimetry as well as satellite synthetic aperture radar, thermal infrared, and visible-range imagery. Spatial and temporal resolution as well as temporal coverage of the GlobCurrent dataproduct is same as those of fields of SLA used in this study.

3.3.3. *Currents by a reanalysis model*

Finally, data on surface currents (at 1.47-m depth) in the region of interest were retrieved from a reanalysis model run by Istituto Nazionale Geologia e Vulcanologia (INGV), Italy. The product is being distributed by CMEMS. Spatial resolution of the data is 0.0625° (approx. 5.3 km per 6.9 km); the same temporal coverage is chosen as for the other two datasets, namely from 1993 to 2015.

4. Mesoscale eddy statistics derived by different techniques

4.1. *Thermal infrared imagery*

In the SST imagery of the Western Mediterranean obtained for the study period (namely the years of 2008 and 2014), a total of 1624 anticyclonic and 522 cyclonic eddy manifestations were detected. Locations of anticyclonic and cyclonic eddies found in the imagery are shown in Fig. 3(a) and (b), respectively. In these plots, marker colour indicates the season in which an eddy was detected. Thus, the dark blue and violet colours refer to the beginning of a year, while pinkish ones indicate the end of a year.

From the way anticyclonic eddy manifestations are spatially distributed we note two tendencies (Fig. 3(a)). First, in the southern half of the region of interest there were more manifestations found than in the northern one. Second, locations of eddies marked the paths of main currents in the study area, namely (i) the Algerian Current, (ii) the Northern Current (that is mostly valid for the Balearic Sea and the Gulf of Lion; in the Liguro-Provençal Basin, eddy structures appear as well, but they are smaller in the spatial scale than those considered in this study (Karimova, 2017b));, (iii) propagation of water from the Liguro-Provençal to the Algerian Basins, and (iv) a large-scale cyclonic gyre in the Tyrrhenian Sea. As far as temporal distribution of the manifestations is concerned, the tendency is that most manifestations were observed during the warm period of a year (Fig. 3(a)). We have to admit that at least partly that happened owing to less frequent appearance of clouds in spring and summer seasons.

Similar to anticyclonic eddies, cyclonic ones found in SST imagery also manifested locations of the main currents, but to a smaller extent, since there were much less cyclones found than anticyclones (Fig. 3(b)). The area with particular frequent appearance of big cyclones was revealed in the near-coastal zone approximately in the middle of the Algerian Basin (Fig. 3(b)). In that area, the instability of the Algerian Current reaches its maximum giving rise to large eddies of both signs of rotation. As for seasonal distribution of cyclonic eddies, relatively great number of cyclonic eddies (in comparison with anticyclonic ones) were found during the cold season as well. Supposedly that happens due to relatively smaller spatial scale of cyclonic eddies which thus require smaller cloud-free gaps for their observation. For further information, the reader is referred to a plot with monthly numbers of eddy manifestations shown in Fig. 5.

Absolute counts of eddy diameters for cyclonic and anticyclonic eddies are shown in Fig. 4(a). The histograms provided indicate that in general cyclonic eddies were smaller than anticyclonic ones. Thus, the most frequent diameter of cyclones referred to the bin of 45–50 km, while that of anticyclones was at the bin of 55–60 km (Fig. 4(a)). The average diameter of cyclonic eddy manifestations was about 54.6 km, while on average anticyclonic eddies were about 76.3 km in diameter. The biggest eddies observed in the study (which were anticyclonic) reached the size of about 175 km in diameter.

It is noteworthy that in reality the dominance of anticyclonic eddies of the spatial scales considered in this study over cyclonic ones can be even greater than it was captured by the histogram in Fig. 4(a). We can claim that due to reported cases of sinking of warm-core anticyclonic vortices as a result of the heat exchange with the atmosphere, etc. (Chapman and Nof, 1988).

As it was mentioned earlier, the presence of cloud cover might significantly affect appearance of eddy manifestations in SST imagery. In our particular case, during the first half of a year there were much more manifestations found than during the second one (Fig. 5).

From different turbulent regimes typical for the study area during the warm and cold seasons one could expect encountering greater average eddy size for the warm period than for the cold period. Plotting values of the monthly averaged eddy diameter (Fig. 5) reveals that that was the case indeed and during the warm season average eddy diameter of anticyclonic eddies was greater than during the cold one. We further note that on average anticyclonic eddies were bigger than cyclonic ones throughout all the year (Fig. 5).

4.2. *Fields of SLA*

In the present subsection, we will check whether the locations of mesoscale eddies found in SST imagery were associated with some local extremums in corresponding fields of SLA, as it is traditionally implied while exploiting altimetry-derived products for mesoscale eddy detection (Chaigneau et al., 2008, 2009; Chelton et al., 2011).

Since distribution of SLA values within a certain area is not necessary centered around zero, introducing any threshold for the values of SLA would automatically exclude a possibility of detecting some significant numbers of closed contours which might refer to eddies. Hereafter we therefore applied a non-threshold approach for extracting locations of possible eddy manifestations from fields of SLA.

As far as the technical procedure is concerned, extraction of possible eddy manifestations was performed in the following way. First, for all SLA fields used in this study the closed-contour plots were constructed with a 0.01-m contour interval. Second, the contours were subdivided into possible manifestations of anticyclonic and cyclonic eddies according to the sign of local SLA anomaly inside the contour (which is expected positive for anticyclones and negative for cyclones).

Absolute counts of diameters of extracted contours are shown in Fig. 4(b). We note that in general diameter values of closed contours of SLA are greater than those of eddy manifestations seen in fields of SST (Fig. 4(a)). For that reason, there was an upper limit introduced for the diameter of closed contours chosen for further consideration. Based on the data of Fig. 4(a), such a limit was established at 150 km.

Another noteworthy point concerning the distribution of diameters of closed contours in Fig. 4(b) is that, unlike the distribution of directly seen eddy diameters (Fig. 4(a)), the number of ‘cyclonic’ contours is just slightly less than that of ‘anticyclonic’ ones. This symmetry in appearance of ‘anticyclonic’ and ‘cyclonic’ contours is possibly the reason for similar statistics of anticyclonic and cyclonic eddies being frequently mistakenly reported for the Western Mediterranean based on an analysis of SLA data (Isern-Fontanet et al., 2006; Escudier et al., 2016).

On having all possible eddy manifestations extracted, we got a chance to check whether there were any corresponding contours of SLA in the vicinity of eddy locations found in SST imagery. The results of such a check are shown in Fig. 6(a) and (b) for anticyclonic and cyclonic eddies, respectively. In these plots, there are the absolute counts of eddy diameters shown for all eddies found in SST fields (outer histograms) and only for those which had corresponding closed contour in the field of SLA (inner histograms); the ratio of the latter to the former is shown with a solid line.

According to Fig. 6(a), manifestation of anticyclonic eddies by local anomalies of SLA significantly depended on the eddy size. Thus, larger eddies were more frequently manifested by closed contours of SLA than smaller eddies. On average, about 36.5% of anticyclonic eddies had corresponding contours of SLA.

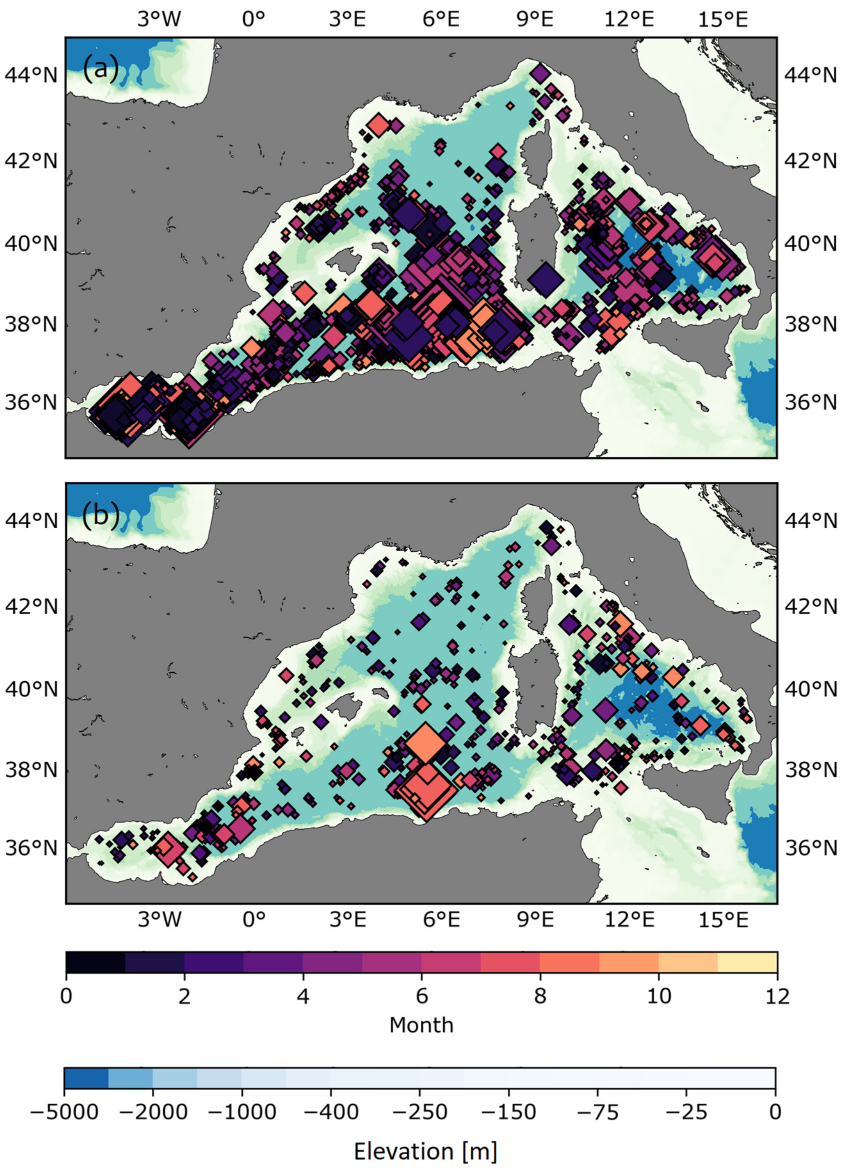

Fig. 3. Locations of anticyclonic (a) and cyclonic (b) eddy manifestations found in L3S SST images during 2008 and 2014. Markers' colour indicates the month when an eddy was observed.

For cyclonic eddies, such dependence of eddy 'visibility' in fields of SLA on the eddy spatial scale was much less persistent, and mainly the detectability of eddies by contours of SLA was directly proportional to the appearance of such eddies in fields of SST (Fig. 6(b)). On average, 13.2% of cyclonic eddies seen in SST had corresponding closed contours of SLA. Such great disagreement between SST and SLA signals must be accounted for by smaller spatial scales of cyclonic eddies comparing to those of anticyclones, due to which cyclonic eddies practically could not be 'sensed' by gridded fields of SLA.

In order to reveal in which period of a year the relationship between eddy manifestations in fields of SST and SLA was closest, in Fig. 6(e) and (f), there are plots provided similar to the previously discussed ones (Fig. 6(a) and (b)), but showing dependence on a calendar month instead of the eddy spatial scale. We note that for anticyclonic eddies, the highest accordance between eddy manifestations in SST and contours of SLA was achieved in July and August, which resulted in the confirmation fraction of about 0.5 (Fig. 6(e)). As it was mentioned earlier, during summer months eddies reach their largest size (Fig. 5) and supposedly the highest degree of geostrophic balance as well. As for cyclonic eddies, there were no strong seasonal dependences revealed (Fig. 6(f)).

Now we will have a look at spatial variabilities of eddy manifestation by closed contours of SLA as well. In Fig. 7(a) and (b), there are once again the plots showing locations of anticyclonic and cyclonic eddies found in the SST imagery. Eddy manifestations for which corresponding closed contours of SLA were found are denoted by violet markers, while markers representing eddies that did not correspond to any closed contour of SLA are marked pink. We note that anticyclonic eddies attributed to the zone of Atlantic water propagation were manifested by contours more frequently than eddies found further north (Fig. 7(a)). Being quite large and long-living, eddies in the southern area apparently had a greater chance of getting manifested in a SLA field. Cyclonic eddies found in fields of SST and manifested by contours of SLA were to a greater extend scattered over the region of interest than anticyclonic ones (Fig. 7(b)). This observation supposedly indicates that the registered cases of coincidence between cyclonic eddy manifestations in fields of SST and SLA were to a certain degree random.

Finally, we will analyse spatial variations of the appearance of closed contours of SLA in the region of interest. Fields of the contour

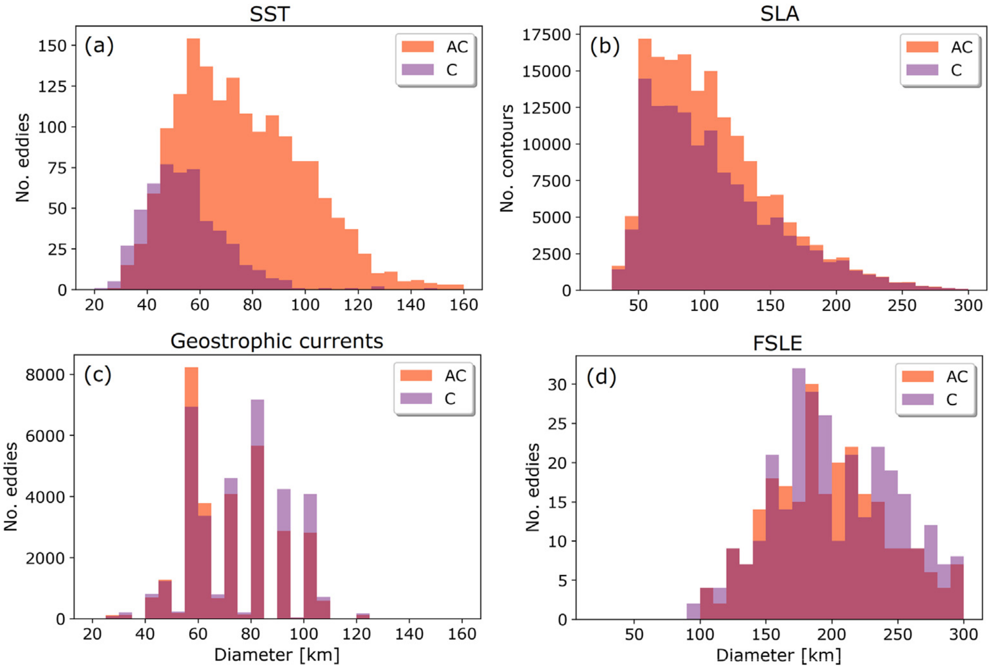

Fig. 4. Absolute counts of diameters of anticyclonic (AC) and cyclonic (C) eddy manifestations (or possible eddy manifestations) extracted from fields of SST (a), SLA (b), geostrophic currents (c), and FSLE (d).

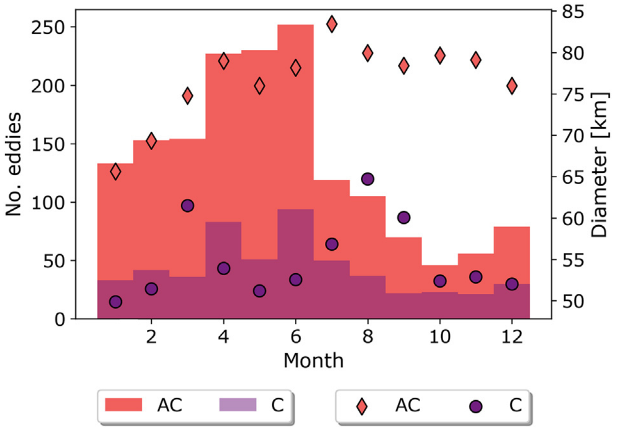

Fig. 5. Monthly-averaged number (bars) and diameter (markers) of eddy manifestations found in fields of SST in 2008 and 2014.

density (number of contours per a grid cell) for 'anticyclonic' and 'cyclonic' contours are presented in Fig. 8(a) and (b), respectively. For 'anticyclonic' contours (Fig. 8(a)), the spatial pattern of the contour density is very close to the scheme of spatial distribution of eddies found in SST imagery (Fig. 3(a)). We can conclude that despite manifestation of individual eddies by contours of SLA might encounter some difficulties, in general such contours seem to represent the spatial distribution of large anticyclonic vortices in the region of interest quite adequately. For further comparison, the reader is referred to works by Pujol and Larnicol (2005) and Isern-Fontanet et al. (2006).

A scheme for the density of 'cyclonic' contours of SLA (Fig. 8(a)) also captures some features of the eddy distribution shown in Fig. 3(b), but in general the coverage of the study area by 'cyclonic' contours is quite homogeneous, which raises a question on possible multiple 'false alarms' presenting among 'cyclonic' contours.

It is important to be aware that so far we were concentrating only on detecting possible locations of eddies. Needless to say that when one would like to extract information on the eddy spatial scale as well based on closed contours of SLA, a particular careful calibration of such a technique is needed, which unfortunately can be not that a straightforward procedure. For more details on extraction of the eddy spatial scale from fields of SLA the reader is referred to (Karimova, 2018).

4.3. Fields of geostrophic currents

In the present subsection, we will perform a similar to the previous one analysis, but for the vector-geometry technique of eddy detection. As working material we will use fields of geostrophic currents calculated from the SLA data analysed in the previous subsection. Generally speaking, some other vector fields of surface currents (e.g. used hereafter data on the total currents provided by the GlobCurrent project) could be applied for eddy detection as well, but we expect that fields of geostrophic currents would provide better results on revealing locations of eddies than the GlobCurrent total currents.

As it was mentioned earlier, in order to extract eddy-like patterns in vector fields of surface geostrophic currents, a methodology proposed by Nencioli et al. (2010) was used. Similar to the closed-contour approach, after extracting possible eddy manifestations, it was checked which of eddy manifestations directly seen in thermal infrared imagery related to an eddy-like pattern in the field of surface currents. The results for anticyclonic and cyclonic eddy manifestations are shown in Fig. 6(c) and (d), respectively. In general, detectability of anticyclonic eddy manifestations in vector fields (Fig. 6(c)) was quite similar to that by closed contours of SLA (Fig. 6(a)), but the overall detectability rate was slightly higher for the vector-geometry technique than for the closed-contour approach and reached 44.9%. For cyclonic eddy manifestations, the situation seemed a bit more optimistic as well (Fig. 6(d)) with the overall eddy detectability rate of 25.1%.

Patterns of the spatial distribution of eddies detected both in fields of SST and geostrophic currents are presented in Fig. 7(c) and (d). These schemes are quite similar to those provided for the closed-contour approach (Fig. 7(a) and (b)), which points to a good agreement between the two methods of eddy detection. If we have a look at the density of all possible eddy manifestations found in vector fields (Fig. 8(c) and (d)), we, however, note that by the vector-geometry method locations of anticyclones along the southern coast of the region of interest were indicated somewhat less persistently (Fig. 8(c)) than it was done by the

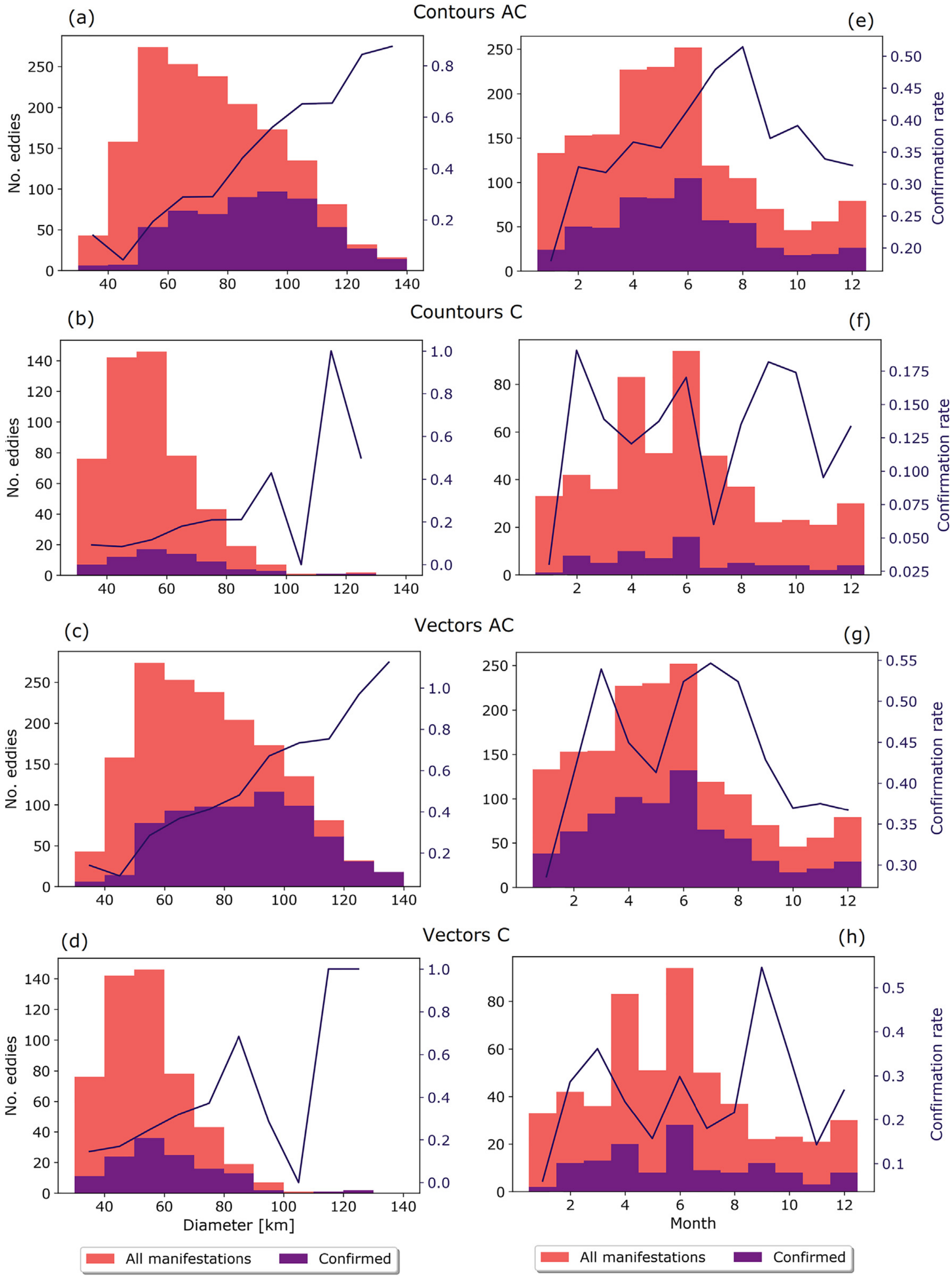

Fig. 6. Bars: absolute counts of anticyclonic (a, c, e, g) and cyclonic (b, d, f, h) eddy manifestations of different spatial scales found in fields of SST and SLA (a, b) and SST and geostrophic currents (c, d); (e–h) same as (a–d), but for different months. Solid line: fraction of eddy manifestations confirmed in fields of SLA to the total amount of eddy manifestations found in SST imagery.

closed-contour approach (Fig. 8(a)). We suppose that in vector fields detection of big eddies in the vicinity of the coast can be hindered due to technical reasons (e.g. when a spiral pattern is only partly manifested in the vector field). On the other hand, field of the density of possible cyclonic manifestations managed to capture a chain of eddies along the north-western coast of the region of interest (Fig. 8(d)). This chain was only party represented by closed contours of SLA (Fig. 8(b)), but was clearly manifested in SST imagery (Fig. 3(b)).

Despite there are quite strong potentials of the vector-geometry approach for finding eddy locations, there exist a serious shortcoming of such a technique as well. This concerns an assessment of the spatial scale of an eddy manifestation found in a vector field. The idea of

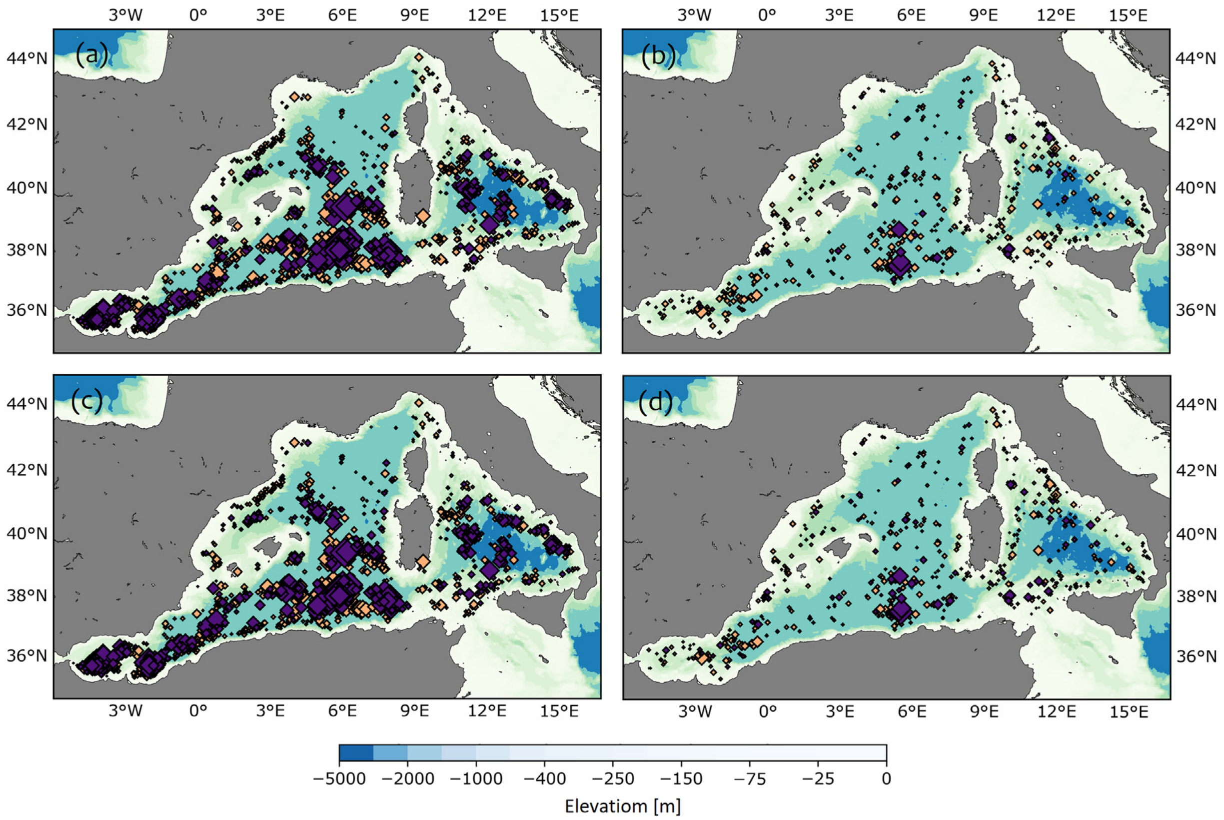

Fig. 7. Locations of anticyclonic (a, c) and cyclonic (b, d) eddies found in fields of SST and SLA (a, b) and in fields of SST and geostrophic currents (c, d). If an eddy was found in the field of SLA as well, it was marked purple, if only in SST, it was left yellow. (For interpretation of the references to color in this figure legend, the reader is referred to the web version of this article.)

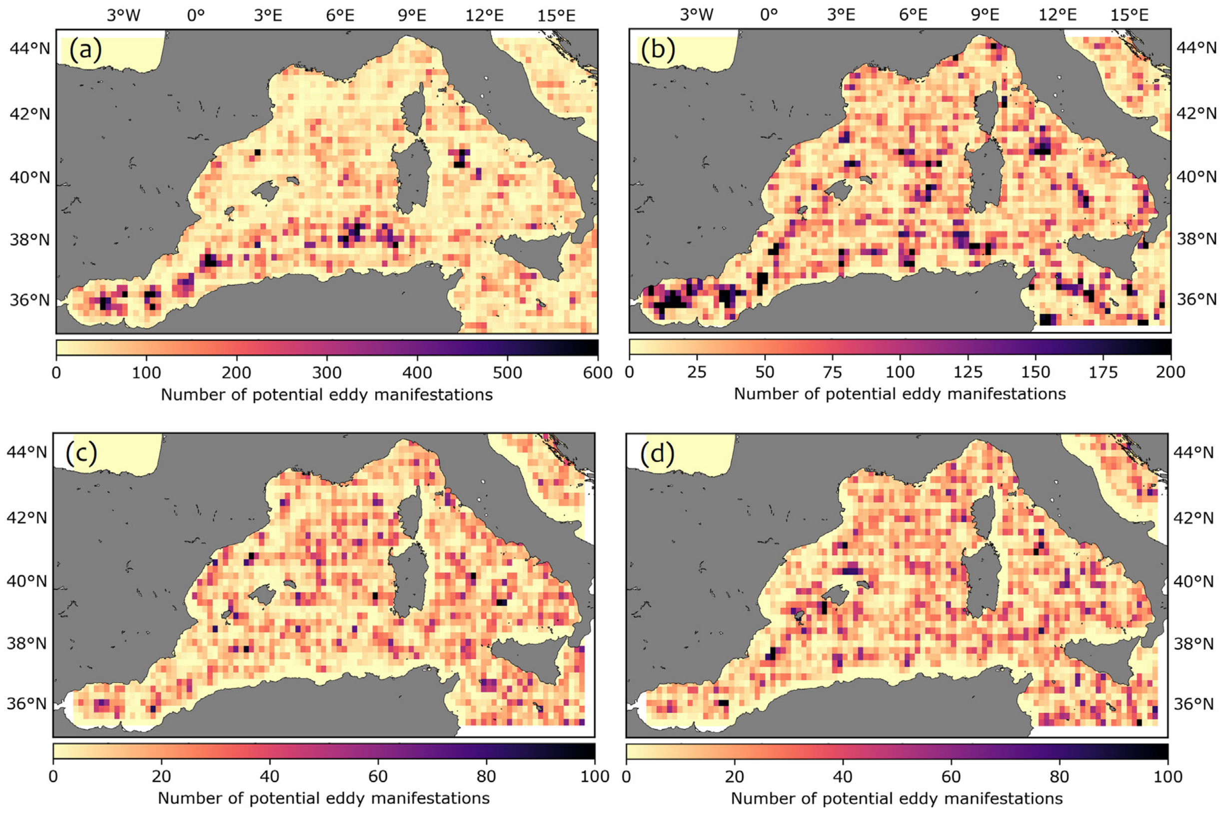

Fig. 8. Number of ‘anticyclonic’ (a, c) and ‘cyclonic’ (b, d) closed contours of SLA (a, b) and eddy-like vector patterns (c, d) per a grid cell for 2008 and 2014.

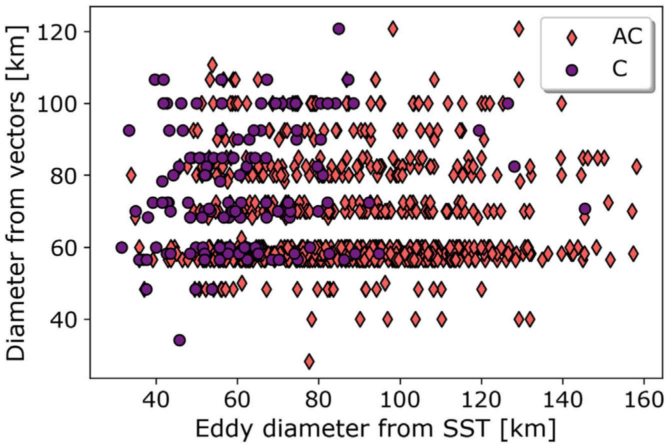

Fig. 9. Values of eddy diameters directly extracted from fields of SST plotted versus values assessed based on fields of geostrophic currents.

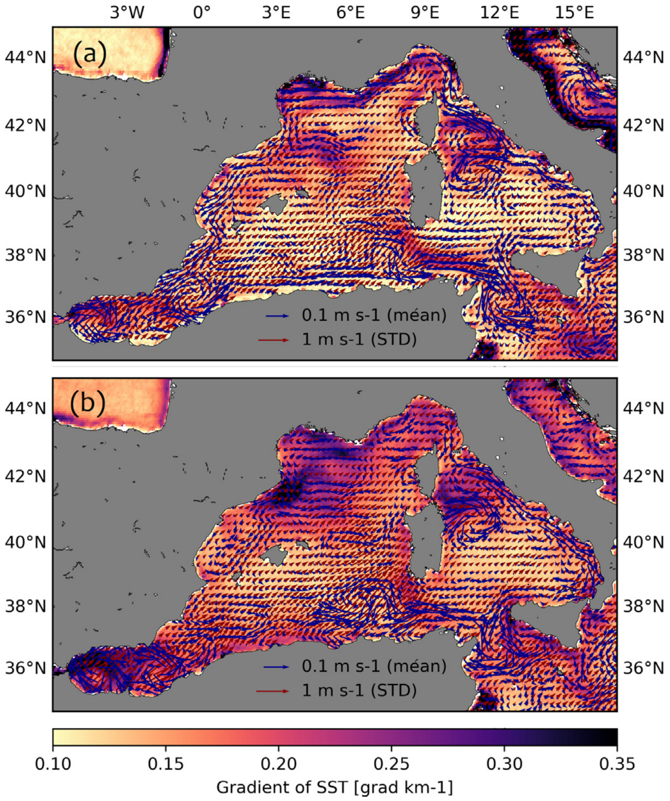

Fig. 10. Fields of seasonally averaged numerical gradient of SST (colour shading), geostrophic currents (blue arrows), and STD of geostrophic currents (red arrows) for the cold (a) and warm (b) seasons. (For interpretation of the references to colour in this figure legend, the reader is referred to the web version of this article.)

establishing the outer border of an eddy at the places with the maximum amplitude of the current velocity seems quite logical and elegant (even though this technique would automatically underestimate the size of an eddy due to disregarding its peripheral part), but can encounter certain difficulties in practice. Frequently such maximum speed of surface currents is associated with a flow next to the eddy under consideration, which can lead to an overestimation of the eddy diameter. For that reason, the distance within which potential eddy periphery is being searched should be reasonably limited. In its turn, such a limitation would cause underestimation of the spatial scale of eddies exceeding the established limit.

Another difficulty can appear in case of the low spatial resolution of vector fields being analysed. In our case the grid spacing was about 12 km, so even in the ideal case the eddy diameter could not be assessed with better precision than this grid size value.

Fig. 9 illustrates the problems just outlined. It shows the assessed values of eddy diameters retrieved by the vector-geometry approach plotted versus the values directly gained from SST imagery. The plot indicates that there was some sensitivity of the ‘real’ eddy spatial scale demonstrated by cyclonic eddy manifestations. For anticyclonic ones, however, assessed values of eddy diameters did not demonstrate any sensitivity of the eddy size directly gained from SST images (Fig. 9).

The absolute counts of all eddy diameters extracted from fields of geostrophic currents can be found in Fig. 4(c). This histogram indicates that there were similar numbers of cyclones and anticyclones found within certain ranges of spatial scales; for larger scales, there was even some dominance of cyclonic eddies observed (Fig. 4(c)). Taking into account the evidence derived from SST imagery (Fig. 4(a)), such results seem quite unrealistic. Possible reasons for such a discrepancy between the results provided by different eddy detection techniques deserve a consideration in further studies.

4.4. Fields of FSLE

As a final step of the comparison undertaken an analysis of eddy manifestations seen in fields of FSLE was performed. Such fields frequently provide impressive manifestations of large vortical structures in the study area (Fig. 2(c) and (d)). If we, however, compare such fields with simultaneously obtained satellite imagery, e.g. fields of Chl-a shown in Fig. 2(a) and (b), we note that (i) fields of FSLE did not resolve smaller spatial scales and (ii) even large anticyclonic and cyclonic vortices were not always adequately represented in fields of FSLE. Thus, unlike the results provided by SST imagery, a more careful look at vortical structures visualized by FSLE yielded dominance of large cyclones over anticyclones. The absolute counts of eddy diameters extracted from fields of FSLE are shown in Fig. 4(d). This histogram reports on the presence of eddies in the range of diameters 100–400 km with slight dominance of large cyclones. According to the eddy statistics retrieved from SST images and used hereafter as the reference data (Fig. 4(a)), eddy manifestations shown by fields of FSLE have very limited connection to reality. Based on these preliminary results, a detailed comparison of manifestations found in such fields with ones from satellite imagery was found unnecessary.

5. Basin-scale surface circulation

This section is devoted to an analysis of general surface circulation in the region of interest shown by different products on surface currents. In particular, we will consider fields of seasonally averaged surface currents from the three datasets being under consideration for the entire period of the study, namely from 1993 to 2015. Upon a preliminary analysis of seasonal variability of surface circulation in the region of interest it was revealed that most notable differences existed between the cold and warm seasons. So hereafter we will define the cold season as a period from October to March and the warm one, from April to September.

Figs. 10–12 show fields of seasonally averaged surface currents according to the SLA, GlobCurrent, and reanalysis datasets described in Section 3.3, respectively. In these figures, blue arrows refer to the average values of the speed of surface currents, while red ones represent the corresponding values of the standard deviation (STD). We note that the currents in the region of interest are quite variable and thus values of STD are frequently comparable to those of the mean speed of surface currents. Interestingly enough, zonal and meridional components of STD seem comparable as well, despite the strongest flows in the area are mostly zonally oriented (Figs. 10–12).

In order to facilitate an assessment of the influence of thermal

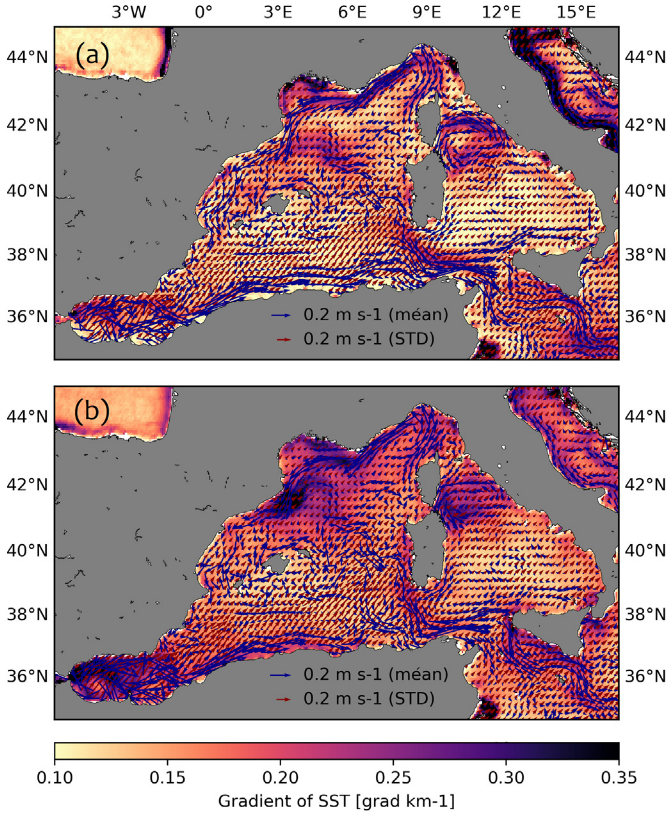

Fig. 11. Fields of seasonally averaged numerical gradient of SST (colour shading), total currents by the GlobCurrent project (blue arrows), and STD of GlobCurrent currents (red arrows) for the cold (a) and warm (b) seasons. (For interpretation of the references to color in this figure legend, the reader is referred to the web version of this article.)

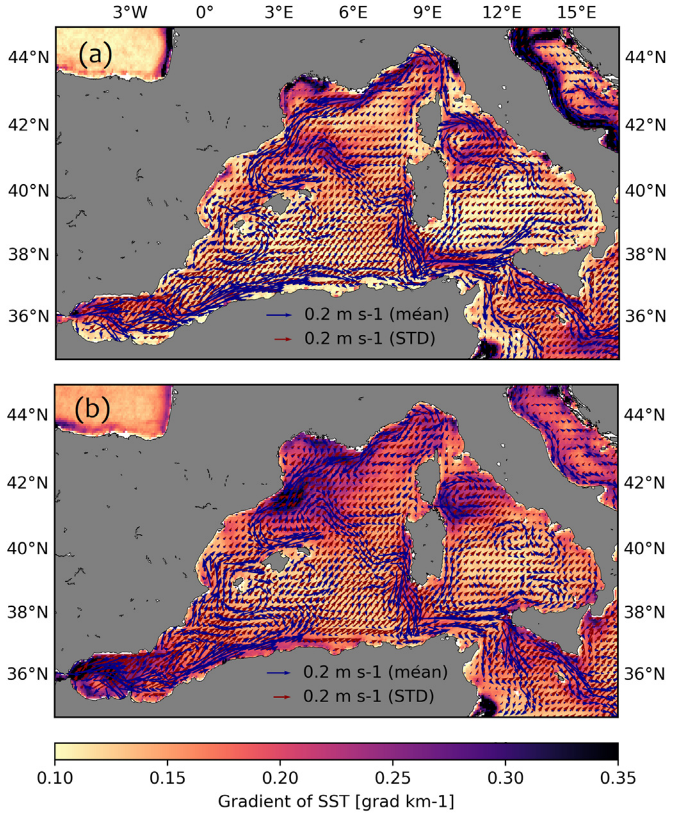

Fig. 12. Fields of seasonally averaged numerical gradient of SST (colour shading), surface currents by the reanalysis (blue arrows), and STD of reanalysis currents (red arrows) for the cold (a) and warm (b) seasons. (For interpretation of the references to color in this figure legend, the reader is referred to the web version of this article.)

frontal zones on the routes of main surface currents, background colour shading in Figs. 10–12 indicates seasonally averaged fields of numerical gradient of SST for the study period (2008–2015). According to these fields, sharpest thermal zones in the study area are associated with (i) the Alboran Eddies, (ii) the Northern Current, (iii) the small cyclonic gyre in the northern Tyrrhenian Sea (hereafter Northern Tyrrhenian Gyre), (iv) the Balearic Current, and (v) a flow from the Western to the Eastern Mediterranean Basins (Fig. 10). More information on hydrological fronts of the Western Mediterranean Basin observed in satellite-derived fields can be gathered in (Karimova, 2017b, 2017c).

Fields of seasonally averaged geostrophic currents retrieved from SLA data are presented in Fig. 10. Among most persistent currents captured by such fields, there are (i) the Northern Current, which is traceable practically along the entire northern coast of the Western Mediterranean, (ii) the outflow of modified Atlantic water through the Strait of Sicily, and (iii) near-coastal flow in the northern Tyrrhenian Sea (Fig. 10).

Due to their nature, fields of geostrophic currents quite clearly show the locations of persistent anticyclonic eddies in the region of interest. Thus, the schemes in Fig. 10 indicate that both Alboran Eddies were particularly well manifested during the warm season (Fig. 10(b)). A large gyre just next to the Alboran Eddies seems quite persistent as well, especially during the cold season (Fig. 10a). In the northern part of the Western Mediterranean, the most frequently observed eddy, according to the fields of geostrophic currents, is the Northern Tyrrhenian Gyre. This eddy was marked in the scheme by Millot (1999) as wind-induced (namely originated from wind forcing coming through the Bonifacio Strait). Among more recent schemes of general surface circulation, this gyre was mentioned by Poulain et al. (2012) and highlighted in a scheme of averaged surface currents in (Pinardi et al., 2015). In our schemes of seasonally averaged geostrophic currents, the eddy was manifested during both seasons; northwards of this cyclonic gyre there is another one with the anticyclonic sign of rotation (Fig. 10).

Concerning total currents assessed by the GlobCurrent project (Fig. 11), we note that, similar to the data on geostrophic currents, fields from the GlobCurrent dataset highlighted the Northern Current, the Algerian Current, and the outflow into the Eastern Mediterranean Basin; these flows were almost equally strongly expressed during the cold and warm seasons. Unlike the schemes of geostrophic currents, the GlobCurrent fields manifested the propagation of Atlantic water as one concentrated stream rather than a strongly meandering and instable flow. Another difference with the fields of geostrophic currents noted upon the comparison is that the strongest currents present in the GlobCurrent schemes are in a good accordance with main thermal frontal zones (Fig. 11). This observation is particularly valid for the Northern Current in the Liguro-Provençal Basin and the Balearic Sea. In a similar way, the Northern Tyrrhenian Gyre is well aligned with the thermal zones rather than with features of SLA and corresponding geostrophic currents (one should compare Fig. 10 and 11). Such a good accordance of surface currents directions with major thermal fronts apparently indicates that ongoing studies on possible synergies between altimetry-derived datasets and satellite imagery (most frequently fields of SST) can be a very fruitful and potential approach (e.g. Nencioli and Quartly, 2018; Rio and Santoleri, 2018).

One more remarkable feature of the fields of averaged total currents by GlobCurrent in Fig. 11 is that these fields captured almost no seasonal changes in the intensity of surface circulation. It is known, however, that seasonal variability of surface currents is quite significant in the study area. Thus, during the warm season, the main currents are expected to be less straightforward than during the cold period, while eddies are supposed to be more developed during the warm period (Send et al., 1999). The dataset on geostrophic currents, according to Fig. 10, seems to perform slightly better in this respect, showing some seasonal changes in the strength of surface circulation.

Finally, fields of seasonally averaged surface currents provided by the reanalysis are presented in Fig. 12. A very remarkable feature of such fields is that they clearly demonstrated the eastward turn of the Northern Current and the origination of the Balearic Current north of the Balearic Islands (Fig. 12). This change of the direction of the main along-coastal current (namely the Northern Current) was highlighted by the geostrophic and GlobCurrent datasets as well (Figs. 10 and 11), but not as distinctively as by the reanalysis fields. The presence of such a turn indicates that in the northern part of the Western Mediterranean (comprising the Balearic Sea and the Liguro-Provençal Basin) there exists a cyclonic gyre (hereafter for convenience 'Provençal Gyre'), which is being completed on the eastern side by the Western Corsican Current. According to the reanalysis method, the Western Corsican Current is shown as quite weak (Fig. 12). The GlobCurrent dataset, however, presented this flow rather strong and associated with a prominent thermal zone (Fig. 11). Location of the Provençal Gyre is shown quite uniform during both cold and warm seasons (Fig. 12).

We also note that shown here fields of surface currents by reanalysis are very close to those presented by Pinardi et al. (2015) obtained for the period 1987–2007. The main difference between the two is that the latter indicate a strong northward flow along the western coast of the Western Mediterranean Basin, while the former rather highlighted the retroflections of the Northern and Algerian Currents to the north and south from the Balearic Islands, respectively (Fig. 12). The presence of this northward flow is quite a questionable point, since two other datasets of the study (namely geostrophic and GlobCurrent currents) as well as most conventional generalized schemes of surface circulation (e.g. by Buffett et al. (2013), Gogou et al. (2014), Millot (1987, 1999), Poulain et al. (2012), Tomczak and Godfrey (2003)) show cyclonic circulation along the entire coast. Such a situation with strong southward near-coastal flow can be particularly clearly observed in the cold-season field of averaged geostrophic currents (Fig. 10(a)).

In order to further highlight the differences between the surface circulation patterns revealed, in Fig. 13 there are seasonally averaged surface currents by all three datasets shown in the same plot. In these plots, geostrophic fields and those by GlobCurrent are given at their full grid, while reanalysis data were double-spaced. Once again we note that geostrophic data mostly indicated locations of eddies and small gyres, which are often being 'sensed' by fields of SLA. Field of average surface currents provided by GlobCurrent and the reanalysis frequently ignored the presence of quasi-permanent eddies and mostly showed strait flows in the region of interest (Fig. 13). In general, average currents from the reanalysis are quite consistent with those from GlobCurrent. There are just some minor differences between the two. First, during the warm season the GlobCurrent data were a bit uncertain about the path of the Algerian Current in the area to the south-west of Sardinia, due to significant meandering of the flow in that area, while according to the reanalysis data, the flow was getting inflicted northwards and merged with the Provençal Gyre. Another difference between the fields provided by GlobCurrent and the reanalysis is that the former showed the Western Corsican Current to be stronger than the Eastern one, while the latter indicated the opposite. From a careful analysis of satellite imagery of the Liguro- Provençal Gyre, we tend to support the point of view of the GlobCurrent dataset (Karimova, 2017b, 2017c). Based on the examples mentioned, we can conclude that all three datasets are quite complementary and the best representation of surface currents in the region of interest can probably be obtained via intercalibration of the datasets.

If we compare the schemes in Fig. 13 with the previously published ones (e.g. by Buffett et al. (2013), Millot (1987, 1999), Tomczak and Godfrey (2003)), we note a greater number of cyclonic large-scale gyres comparing to the conventional schemes. One of the first publications where a medium-size cyclonic gyre (that was the Provençal Gyre) was mentioned in a generalized scheme of surface circulation was Pinardi and Masetti (2000). Most previous studies did not take into account the Northern Tyrrhenian Gyre. In some other works, gyres in the Tyrrhenian Sea were not shown at all (Millot, 1987, 1999). At times, there is no the Provençal Gyre shown in the scheme (Buffett et al., 2013) or very variable routes of this gyre can be found (Pinardi and Masetti, 2000; Poulain et al., 2012; Tomczak and Godfrey, 2003).

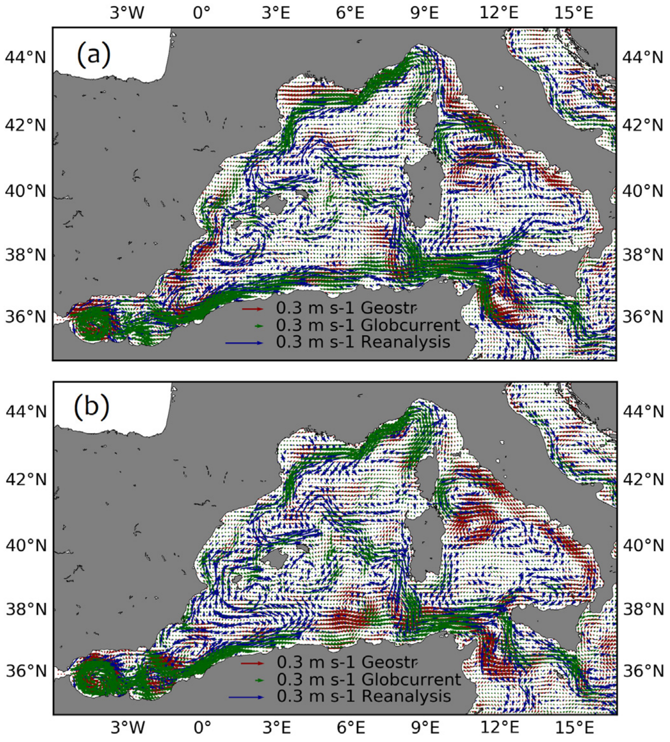

Fig. 13. Fields of seasonally averaged geostrophic, total GlobCurrent, and surface reanalysis currents for the cold (a) and warm (b) seasons.

Interestingly enough, in this study we did not manage to discover the big gyres in the eastern Algerian Basin traced upon experiments with subsurface Lagrangian floats (Testor et al., 2005). Apparently circulation patterns at 600 m depth, where floats were placed, are greater in size and more persistent in time than those observed near the water surface.

One more interesting point concerns the direction of currents around the southern coast of Sardinia. Thus, if any currents are shown to the west of Sardinia in schemes of surface circulation, they are usually indicated as flowing anticyclonically (Buffett et al., 2013; Sverdrup et al., 1944). Based on the evidence gathered in the present study, we tend to believe, however, that the circulation in that area is more likely cyclonical.

In general, results of the present work seem to be very close to the ones derived for geostrophic currents in the entire Mediterranean Sea from drifter and satellite altimeter data (Poulain et al., 2012), even though the analysis of surface currents in that study was performed with lower spatial resolution and thus could not resolve certain fine details like individual quasi-permanent eddies.

6. Conclusions

An analysis undertaken in the study revealed that different eddy detection techniques can provide quite different results. Thus, a visual inspection of the SST imagery indicated anticyclonic eddy dominance in the region of interest both in the number and the size of eddies, while commonly used methodologies of eddy detection in the fields of SLA and geostrophic currents provided similar numbers for cyclones and anticyclones or even showed the prevalence of cyclones. Applying a SLA-based closed-contour approach yielded, however, quite promising results for relatively large (exceeding ca. 70 km in diameter) anticyclonic eddies. Since cyclonic eddies in the region of interest are typically much smaller than anticyclonic ones, adequate detection of cyclones can be facilitated only by satellite imagery of high and medium spatial resolution.

Vortex-like structures seen in the generic fields of FSLE analysed in the study did not seem to correspond to actual gyres observed in other satellite-derived fields of the region of interest.

As far as general surface circulation is concerned, fields of seasonally averaged surface currents from different data sources provided quite different evidence on the patterns of surface circulation in the region of interest. Thus, geostrophic currents retrieved from gridded fields of SLA were mainly highlighting the presence of most persistent and largest eddies in the area, while surface currents provided by the GlobCurrent project manifested both the main currents and frequent locations of largest eddies (such as Alboran Eddies and gyres along the Algerian Coast). Data on surface currents from the reanalysis technique seemed to provide a good representation of the location of the main currents as well. Application of numerical methods to the retrieval of surface currents in the region of interest resulted in avoiding possible unrealistic divergence/convergence of surface circulation and thus a better manifestation of its horizontal cells (e.g. such as the Provençal Gyre). On the other hand, fields of mean surface currents from the reanalysis almost totally ignored the presence of quasi-permanent eddies, even as large ones as Alboran Eddies. We can therefore conclude on the complementarity of those three datasets on surface currents analysed in the study. A combined usage of such datasets would be very beneficial for a better understanding of basin-scale surface circulation in the study area.

The main conclusion of the study is that all techniques being proposed for mesoscale eddy detection and assessment of surface currents based on satellite information require stages of very careful calibration and cross-validation.

Acknowledgements

This research has been supported by the University of Liege and the E.U. in the context of the FP7-PEOPLE-COFUND-BeIPD project. The study has been conducted using E.U. Copernicus Marine Service Information as well as the results of the GlobCurrent project, and data distributed by AVISO +. The author is very grateful to the anonymous reviewers for their careful reading and valuable comments.

References

Barale, V., Jaquet, J.-M., Ndiaye, M., 2008. Algal blooming patterns and anomalies in the Mediterranean Sea as derived from the SeaWiFS data set (1998–2003). Remote Sens. Environ. 112, 3300–3313.

Beron-Vera, F.J., Olascoaga, M.J., Goni, G.J., 2008. Oceanic mesoscale eddies as revealed by Lagrangian coherent structures. Geophys. Res. Lett. 35, L12603. https://doi.org/10.1029/2008GL033957.

Buffett, G.G., Hobbs, R.W., Vsemirnova, E., Klaeschen, D., Hurich, C., 2013. Characterization of thermohaline staircases in the Tyrrhenian Sea using stochastic heterogeneity mapping. J. Acoust. Soc. Am. 133 (5), 3313.

Casella, E., Molcard, A., Provenzale, A., 2011. Mesoscale vortices in the Ligurian Sea and their effect on coastal upwelling processes. J. Mar. Syst. 88, 12–19.

Chaigneau, A., Gizolme, A., Grados, C., 2008. Mesoscale eddies off Peru in altimeter records: identification algorithms and eddy spatio-temporal patterns. Prog. Oceanogr. 79, 106–119.

Chaigneau, A., Eldin, G., Dewitte, B., 2009. Eddy activity in the four major upwelling systems from satellite altimetry (1992–2007). Prog. Oceanogr. 83, 117–123.

Chapman, R., Nof, D., 1988. The sinking of warm-core rings. J. Phys. Oceanogr. 18, 565–583.

Chelton, D.B., Schlax, M.G., Samelson, R.M., de Szoeke, R.A., 2007. Global observations of large oceanic eddies. Geophys. Res. Lett. 34, L15606. https://doi.org/10.1029/2007GL030812.

Chelton, D.B., Schlax, M.G., Samelson, R.M., 2011. Global observations of nonlinear mesoscale eddies. Prog. Oceanogr. 91, 167–216.

D'Ovidio, F., Fernandez, V., Lopez, C., Hernandez-Garcia, E., Garcia-Ladona, E., 2009. Comparison between Eulerian diagnostics and finite-size Lyapunov exponents computed from altimetry in the Algerian basin. Deep-Sea Res. I 56, 15–31.

Escudier, R., Renault, L., Pascual, A., Brasseur, P., Chelton, D., Beuvier, J., 2016. Eddy properties in the Western Mediterranean Sea from satellite altimetry and a numerical simulation. Journal of Geophysical Research Oceans 121, 3990–4006. https://doi.org/10.1002/2015JC011371.

Font, J., Rousseau, S., Shirasago, B., García-Górriz, E., Haney, R.L., 2002. Mesoscale variability in the Alboran Sea: synthetic aperture radar imaging of frontal eddies. J. Geophys. Res. 107 (C6), 3059.

Font, J., Isern-Fontanet, J., Salas, J., 2004. Tracking a big anticyclonic eddy in the western Mediterranean Sea. Sci. Mar. 68 (3), 331–342.

Ginzburg, A.I., Kostianoy, A.G., Krivosheya, V.G., Nezlin, N.P., Soloviev, D.M., Stanichny, S.V., Yakubenko, V.G., 2002. Mesoscale eddies and related processes in the northeastern Black Sea. J. Mar. Syst. 32 (1–3), 71–90. https://doi.org/10.1016/S0924-7963(02)00030-1.

Gogou, A., Sanchez-Vidal, A., Durrieu de Madron, X., Stavrakakis, S., Calafat, A.M., Stabholz, M., Psarra, S., Canals, M., Heussner, S., Stavrakaki, I., Papathanassiou, E., 2014. Carbon flux to the deep in three open sites of the Southern European Seas (SES). J. Mar. Syst. 129, 224–233.

Halo, I., Backeberg, B., Penven, P., Ansorge, I., Reason, C., Ullgren, J., 2013. Eddy properties in the Mozambique Channel: a comparison between observations and two numerical ocean circulation models. Deep-Sea Res. II 100, 38–53.

Henson, S.A., Thomas, A.C., 2008. A census of oceanic anticyclonic eddies in the Gulf of Alaska. Deep-Sea Res. I 55, 163–176.

Isern-Fontanet, J., García-Ladona, E., Font, J., 2003. Identification of marine eddies from altimetry. J. Atmos. Ocean. Technol. 20, 772–778.

Isern-Fontanet, J., García-Ladona, E., Font, J., 2006. Vortices of the Mediterranean Sea: an altimetric perspective. J. Phys. Oceanogr. 36, 87–103.

Karimova, S.S., 2011. Eddy statistics for the Black Sea by visible and infrared remote sensing. In: Tang, D. (Ed.), Remote Sensing of the Changing Oceans. Springer-Verlag, Berlin Heidelberg, pp. 61–76.

Karimova, S., 2013. Non-stationary eddies in the Black Sea as seen by satellite infrared and visible imagery. Int. J. Remote Sens. 34, 8503.

Karimova, S., 2016. Observation of the surface circulation of the Mediterranean Sea from space. In: Proc. ESA Living Planet Symposium 2016. 9–13 May 2016, Prague, Czech Republic. SP-740. ESA Communications, ESTEC, Noordwijk, The Netherlands.

Karimova, S., 2017a. Observations of asymmetric turbulent stirring in inner and marginal seas. Int. J. Remote Sens. 38 (6), 1642–1664. https://doi.org/10.1080/01431161.2017.1285078.

Karimova, S., 2017b. Observing surface circulation of the Western Mediterranean Basin with satellite imagery. In: The International Archives of the Photogrammetry, Remote Sensing and Spatial Information Sciences. Vol. XLII-3/W2, 2017, 37th International Symposium on Remote Sensing of Environment, 8–12 May 2017, Tshwane, South Africa, pp. 97–104. https://doi.org/10.5194/isprs-archives-XLII-3-W2-97-2017.

Karimova, S., 2017c. Surface circulation in the Western Mediterranean shown by a synergy of satellite-derived datasets. In: Proc. SPIE 10422, Remote Sensing of the Ocean, Sea Ice, Coastal Waters, and Large Water Regions 2017. 104220Mhttps://doi.org/10.1117/12.2278638. (3 October 2017).

Karimova, S., 2018. Eddies in the Western Mediterranean seen in thermal imagery and SLA fields. Int. J. Remote Sens. 39 (13), 4304–4329. https://doi.org/10.1080/01431161.2018.1454626.

Karimova, S., Gade, M., 2016. Eddies in the Western Mediterranean seen by spaceborne radar. In: Proceedings of IGARSS 2016, 10–15 July 2016. Beijing, China.

Karrasch, D., Haller, G., 2013. Do finite-size Lyapunov exponents detect coherent structures? Chaos 23 (4). https://doi.org/10.1063/1.4837075.

Kubryakov, A.A., Stanichny, S.V., 2015. Seasonal and interannual variability of the Black Sea eddies and its dependence on characteristics of the large-scale circulation. Deep-Sea Res. I 97, 80–91.

Kurian, J., Colas, F., Capet, X., McWilliams, J.C., Chelton, D.B., 2011. Eddy properties in the California current system. J. Geophys. Res. 116, C08027. https://doi.org/10.1029/2010JC006895.

McGillicuddy Jr., D.J., Robinson, A.R., Siegel, D.A., Jannasch, H.W., Johnson, R., Dickey, T.D., McNeil, J., Michaels, A.F., Knap, A.H., 1998. Influence of mesoscale eddies on new production in the Sargasso Sea. Nature 394, 263–266.

Mill, G.N., da Costa, V.S., Lima, N.D., Gabioux, M., Guerra, L.A.A., Paiva, A.M., 2015. Northward migration of Cape São Tomé rings - Brazil. Cont. Shelf Res. 106, 27–37.

Millot, C., 1987. Circulation in the Western Mediterranean Sea. Oceanol. Acta 10, 143–149.

Millot, C., 1999. Circulation in the Western Mediterranean Sea. J. Mar. Syst. 20, 423–442. https://doi.org/10.1016/S0924-7963(98)00078-5.

Morrow, R., Birol, F., Griffin, D., Sudre, J., 2004. Divergent pathways of cyclonic and anticyclonic ocean eddies. Geophys. Res. Lett. 31, L24311. https://doi.org/10.1029/2004GL020974.

Nencioli, F., Quartly, G.D., 2018. Exploring the synergy between along-track altimetry and tracer fronts to reconstruct surface ocean currents. Remote Sens. Environ. 216, 747–757. https://doi.org/10.1016/j.rse.2018.04.036.

Nencioli, F., Dong, C., Dickey, T., Washburn, L., McWilliams, J.C., 2010. A vector geometry-based eddy detection algorithm and its application to a high-resolution numerical model product and high-frequency radar surface velocities in the Southern California Bight. J. Atmos. Ocean. Technol. 27, 564–579. https://doi.org/10.1175/2009JTECHO725.1.

Nielsen, J.N., 1912. Hydrography of the Mediterranean and adjacent waters. In: Report of the Danish Oceanographic Expedition 1908–1910 to the Mediterranean and Adjacent Waters. 1. pp. 77–192.

Palacios, D.M., Bograd, S.J., 2005. A census of Tehuantepec and Papagayo eddies in the northeastern tropical Pacific. Geophys. Res. Lett. 32, L23606. https://doi.org/10.

1029/2005GL024324.

Pegliasco, C., Chaigneau, A., Morrow, R., 2015. Main eddy vertical structures observed in the four major Eastern Boundary Upwelling Systems. J. Geophys. Res. Oceans 120, 6008–6033. https://doi.org/10.1002/2015JC010950.

Pinardi, N., Masetti, E., 2000. Variability of the large scale general circulation of the Mediterranean Sea from observations and modelling: a review. Palaeogeogr. Palaeoclimatol. Palaeoecol. 158, 153–173.

Pinardi, N., Zavatarelli, M., Adani, M., Coppini, G., Fratianni, C., et al., 2015. Mediterranean Sea large-scale low-frequency ocean variability and water mass formation rates from 1987 to 2007: a retrospective analysis. Prog. Oceanogr. 132, 318–332.

Poulain, P.-M., Menna, M., Mauri, E., 2012. Surface geostrophic circulation of the Mediterranean Sea derived from drifter and satellite altimeter data. J. Phys. Oceanogr. 42 (6), 973–990.

Puillat, I., Taupier-Letage, I., Millot, C., 2002. Algerian eddies lifetime can near 3 years. J. Mar. Syst. 31, 245–259.

Pujol, M.-I., Larnicol, G., 2005. Mediterranean Sea eddy kinetic energy variability from 11 years of altimetric data. J. Mar. Syst. 58, 121–142.

Rio, M.-H., Santoleri, R., 2018. Improved global surface currents from the merging of altimetry and sea surface temperature data. Remote Sens. Environ. 216, 770–785. https://doi.org/10.1016/j.rse.2018.06.003.

Sadarjoen, I.A., Post, F.H., Ma, B., Banks, D.C., 1998. Selective visualization of vortices in hydrodynamic flows. In: Visualization'98: Proceedings, October 18–23, 1998, Research Triangle Park, North Carolina. ACM Press, New York, pp. 419–422.

Salas, J., Millot, C., Font, J., García-Ladona, E., 2002. Analysis of mesoscale phenomena in the Algerian basin from drifting buoys and infrared images. Deep-Sea Res. I 49, 245–266.

Sangrà, P., Pascual, A., Rodriguez-Santana, A., Machin, F., Mason, E., McWilliams, J.C., 2009. The Canary Eddy Corridor: a major pathway for long-lived eddies in the subtropical North Atlantic. Deep-Sea Res. I 56, 2100–2114.

Send, U., Font, J., Krahman, G., Millot, C., Rhein, M., Tintoré, J., 1999. Recent advances in studying the physical oceanography of the western Mediterranean Sea. Prog. Oceanogr. 44, 37–64.

Souza, J.M.A.C., de Boyer Montegut, C., Le Traon, P.Y., 2008. Comparison between three implementations of automatic identification algorithms for the quantification and characterization of mesoscale eddies in the South Atlantic Ocean. Ocean Sci. Discuss. 8, 483–531.

Stegmann, P.M., Schwing, F., 2007. Demographics of mesoscale eddies in the California current. Geophys. Res. Lett. 34, L14602. https://doi.org/10.1029/2007GL029504.

Sverdrup, H.U., Johnson, M.W., Fleming, R.H., 1944. The Oceans: Their Physics, Chemistry, and General Biology.

Taupier-Letage, I., Millot, C., 1988. Surface circulation in the Algerian basin during 1984. Oceanol. Acta 79–85.

Testor, P., Send, U., Gascard, J.-C., Millot, C., Taupier-Letage, I., Beranger, K., 2005. The mean circulation of the southwestern Mediterranean Sea: Algerian gyres. J. Geophys. Res. 110, C11017. https://doi.org/10.1029/2004JC002861.

Tomczak, M., Godfrey, J.S., 2003. Regional Oceanography: an Introduction.

Zatsepin, A., Ginzburg, A., Kostianoy, A., Kremenetskiy, V., Krivosheya, V., Stanichny, S., Poulain, P.-M., 2003. Observations of Black Sea mesoscale eddies and associated horizontal mixing. J. Geophys. Res. 108 (C8), 3246. https://doi.org/10.19/2002JC001390.

Zavala Sanson, L., Provenzale, A., 2009. The effects of abrupt topography on plankton dynamics. Theor. Popul. Biol. 76 (4), 258–267.